BIOCHEMISTRY
including biophysical chemistry & molecular biology

Article

pubs.acs.org/biochemistry

Molecular Model of a Soluble Guanylyl Cyclase Fragment Determined by Small-Angle X-ray Scattering and Chemical Cross-Linking

Bradley G. Fritz, Sue A. Roberts, Aqeel Ahmed, Linda Breci, Wenzhou Li, Andrzej Weichsel, Jacqueline L. Brailey, Vicki H. Wysocki, Florence Tama, and William R. Montfort*

Department of Chemistry and Biochemistry, University of Arizona, Tucson, Arizona 85721, United States

ABSTRACT: Soluble guanylyl/guanylate cyclase (sGC) converts GTP to cGMP after binding nitric oxide, leading to smooth muscle relaxation and vasodilation. Impaired sGC activity is common in cardiovascular disease, and sGC stimulatory compounds are vigorously sought. sGC is a 150 kDa heterodimeric protein with two H-NOX domains (one with heme, one without), two PAS domains, a coiled-coil domain, and two cyclase domains. Binding of NO to the sGC heme leads to proximal histidine release and stimulation of catalytic activity. To begin to understand how binding leads to activation, we examined truncated sGC proteins from *Manduca sexta* (tobacco hornworm) that bind NO, CO, and stimulatory compound YC-1 but lack the cyclase domains. We determined the overall shape of truncated *M. sexta* sGC using analytical ultracentrifugation and small-angle X-ray scattering (SAXS), revealing an elongated molecule with dimensions of 115 Å × 90 Å × 75 Å. Binding of NO, CO, or YC-1 had little effect on shape. Using chemical cross-linking and tandem mass spectrometry, we identified 20 intermolecular contacts, allowing us to fit homology models of the individual domains into the SAXS-derived molecular envelope. The resulting model displays a central parallel coiled-coil platform upon which the H-NOX and PAS domains are assembled. The β_1 H-NOX and α_1 PAS domains are in contact and form the core signaling complex, while the α_1 H-NOX domain can be removed without a significant effect on ligand binding or overall shape. Removal of 21 residues from the C-terminus yields a protein with dramatically increased proximal histidine release rates upon NO binding.

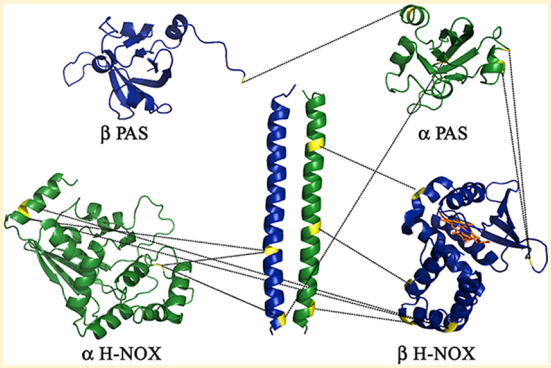

Nitric oxide (NO) regulates numerous vital functions in animal physiology, including blood pressure, memory formation, platelet aggregation, angiogenesis, and tissue development.[1] Dysregulation of NO signaling contributes to cardiovascular disease, cancer, poor wound healing, diabetes, asthma, and aging. NO is produced through the conversion of L-arginine to L-citrulline by nitric oxide synthase (NOS)[2,3] and may function in the cell where it is produced or in nearby cells (autocrine/paracrine signaling). The primary NO receptor is soluble guanylyl/guanylate cyclase (sGC), an ∼150 kDa heterodimeric protein that binds NO through a ferrous heme.[4] NO binding stimulates cyclase activity, the production of cGMP from substrate GTP, and the subsequent amplification of NO-dependent signaling cascades. In smooth muscle cells, this leads to a reduction in the free cytosolic calcium concentration and smooth muscle relaxation, a mechanism closely tied to the regulation of blood pressure. While regulation of NOS is relatively well studied,[5] the mechanisms underlying sGC regulation are poorly understood.[6]

Improving blood flow and lowering blood pressure in cardiovascular disease, the number one cause of death in the Western world, have long been treatment goals. While some success has been achieved, only ∼43% of those treated for hypertension have their condition under control.[7] Overall, 36% of the adult population suffers from cardiovascular disease, a value that increases to 72% for those over age 60 and >80% for those over age 80. Because nitric oxide both lowers blood pressure and improves blood flow through its vasorelaxation and antiplatelet activities, NO signaling has long been a target for treating cardiovascular disease. For example, organic nitrates such as nitroglycerin, which is metabolized to release NO, have a >130 year history in treating angina pectoris.[8] While current treatments are successful for some patients, some do not respond, and many who do then develop tolerance to the compounds, which become ineffective.

Efforts to discover new treatments are increasingly focused on sGC, which is compromised in all forms of cardiovascular disease. One promising avenue for treatment involves compounds related to YC-1, a benzylindazole derivative, which stimulate sGC directly and act synergistically with NO binding.[9] Several such compounds have entered preclinical or clinical trials, one of which (Riociguat) has reached phase III clinical trials.[10,11] While YC-1 family compounds provide a promising step forward, how they bind to sGC and how they stimulate catalytic activity

Received: November 21, 2012
Revised: January 29, 2013

dx.doi.org/10.1021/bi301570m | *Biochemistry* XXXX, XXX, XXX−XXX

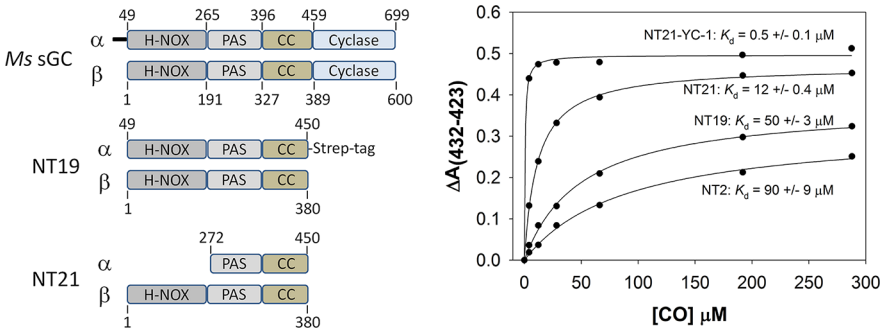

Figure 1. *Ms* sGC domain boundaries, expression constructs, and equilibrium CO titration measurements. Shown are the predicted domain boundaries and boundaries for constructs NT19 and NT21. Not shown are constructs NT1 (α_1 1−471, β_1 1−401), NT2 (α_1 49−471, β_1 1−401), and NT13 (same as NT19 but without the *Strep* tag). Representative saturation binding curves. NT21 responds to YC-1 with a 6-fold tightening of the CO dissociation constant. Also examined were NT2 with YC-1 ($K_d^{CO/YC-1} = 1.0 \pm 0.1$), NT13 ($K_d^{CO} = 42 \pm 5$), NT13 with YC-1 ($K_d^{CO/YC-1} = 0.9 \pm 0.1$), and NT19 with YC-1 ($K_d^{CO/YC-1} = 0.8 \pm 0.1$).

are unknown. A second promising avenue involves compounds targeted to oxidized sGC, which loses heme during inflammation and is then degraded.[12,13] The new compounds replace missing heme, stimulate activity, and stabilize the protein, preventing degradation.

The most common form of sGC is a heterodimeric enzyme with one α_1 subunit of ∼77 kDa and one heme-containing β_1 subunit of ∼70 kDa; α_2 and β_2 subunits also occur with an $\alpha_2\beta_1$ complex that is particularly important in the brain.[4,14] Each subunit consists of four domains: an N-terminal H-NOX (heme-nitric oxide/oxygen binding) domain,[15] a central PAS (Per-ARNT-Sim) domain,[16] a coiled coil, and a C-terminal catalytic domain. Binding of NO to the ferrous *b*-type heme in the β_1 H-NOX domain leads to dissociation of the proximal histidine and stimulation of cyclase activity. Binding of carbon monoxide (CO) can also stimulate sGC upon binding; however, stimulation is weak in the absence of YC-1 or related compounds and, importantly, does not require proximal histidine dissociation.[17,18]

Understanding of NO, CO, and YC-1 allosteric stimulation of sGC is impeded by the lack of sGC crystal structures. Insight can be gained through homology models for individual domains based on crystal structures of bacterial homologues. The H-NOX domain has been most heavily studied in this regard with crystal structures determined for the H-NOX domain from *Thermoanaerobacter tengcongensis*[19,20] and *Nosotoc* sp.[21] The crystal structure of the PAS domain from *Nostoc punctiforme*, which is highly homologous with the sGC PAS domains, has also been determined.[22] Additionally, the structure for a β_1 coiled-coil homodimer from rat has been determined,[23] and the structure of the α_1/β_1 heterodimeric cyclase domain is available (Protein Data Bank entry 3UVJ, unpublished). However, the arrangement of these domains in sGC and the mechanism by which binding of stimulatory molecules leads to activation remain unknown.

We have developed truncated forms of guanylyl cyclase from the tobacco hornworm/hawkmoth (*Manduca sexta*) for biophysical study.[24−26] *Ms* sGC is highly homologous to mammalian sGC proteins and responds to NO, CO, and YC-1 compounds. Constructs lacking the α_1/β_1 catalytic domains can be bacterially expressed, leading to heterodimeric protein that is fully loaded with ferrous heme and which displays the expected heme spectra and ligand binding properties. Of particular interest is the fact that C-terminally truncated *Ms* sGC retains an allosteric response to YC-1 family compounds. Binding of YC-1 or BAY 41-2272 leads to an apparent closing of the heme pocket and enhanced CO and NO binding.[25] Here, we have investigated domain−domain contacts in truncated *Ms* sGC using chemical cross-linking and high-resolution mass spectrometry and determined a molecular envelope for the protein using small-angle X-ray scattering (SAXS). These data have allowed us to assemble the first model for heterodimeric sGC and to probe the mechanism underlying allosteric regulation.

MATERIALS AND METHODS

Design and Cloning of *Ms* sGC Constructs. Several C-terminal truncations of *M. sexta* $\alpha_1\beta_1$ sGC were utilized in this study (Figure 1). The N-terminal construct containing α_1 49−450 and β_1 1−380, termed *Ms* sGC NT13, was expressed in *Escherichia coli* from a pET-Duet-1 vector as previously described.[26] Construct *Ms* sGC NT19 contains the same α_1 and β_1 sequence as NT13 but has an additional C-terminal *Strep* purification tag (WSHPQFEK) on the α subunit. This was cloned by polymerase chain reaction (PCR) amplification from the *Ms* sGC NT13 template using forward primer 5′-gatcggcgtggctagcttctgcaaagcgtttccatggc-3′ and reverse primer 5′-gcgagcaaagcagtagacaaggaacgagagaagacctggagccacccacaattcgaaaaatgaaagcttagcctt-3′. The PCR product was cloned into the p-GEM T Easy vector, removed with restriction endonucleases NheI and HindIII, and subsequently ligated into the pETDuet-NT13 construct using the same restriction enzymes. The final construct, pETDuet-NT19, was transformed into pLysS cells. We prepared construct *Ms* sGC NT21, which lacks the α_1 H-NOX domain, by first excising the α_1 subunit from the *Ms* sGC NT13 pETDuet-1 vector with restriction endonucleases BamHI and NotI, purifying the sample on a 1% agarose gel, excising the 6.6 kb gel band, and purifying the sample with a GeneJET Gel Extraction Kit (Fermentas). The α_1 subunit of residues 272−699 from construct CT1 (unpublished data[a]) was excised with BamHI and NotI, gel purified, and ligated into the pETDuet-1 vector containing NT13 β_1 using a rapid DNA ligation kit (Thermo Scientific). A stop codon was inserted into the CT1 α_1 sequence at position 451 using primer 5′-caaggaacgagagaagtaagtcagcctgctgcatttaatattcc-3′. Sequencing with pETDuet-1 primers UP1 (5′-atgcgtccggcgtaga-3′) and UP2 (5′-ttgtacacggccgcataatc-3′) confirmed the appropriate sequence for expression of α_1 272−450 and β_1 1−380.

Purification of Recombinant *M. sexta* sGC from *E. coli*. *Ms* sGC NT13, NT19, and NT21 were expressed in *E. coli* and purified by a previously described procedure[24,26] with the following modifications. NT19 was expressed at 30 °C in

dx.doi.org/10.1021/bi301570m | *Biochemistry* XXXX, XXX, XXX−XXX

BL21(DE3)pLysS cells and lysed with a French press, and the resulting supernatant was applied to a prepacked Ni^{2+}-NTA affinity column (GE Healthcare, Piscataway, NJ). Protein was eluted from the Ni^{2+}-NTA resin with 30 mM EDTA, loaded directly onto a StrepTactin Sepharose High Performance column (GE Healthcare), washed with equilibration buffer, eluted in approximately 1 mL of equilibration buffer containing 2.5 mM desthiobiotin, and loaded onto a Sephacryl S-200 gel filtration column (GE Healthcare). NT21 was expressed optimally from Rosetta(DE3)pLysS cells at 16 °C while they were being shaken at 90 rpm for 15 h. Purification was like that described for NT13, using Ni^{2+}-NTA and size exclusion chromatography. All gel filtration steps for NT13, NT19, and NT21 included 1 mM tris(2-carboxyethyl)phosphine (TCEP) as a reductant to prevent aggregation.

Analytical Ultracentrifugation. Sedimentation velocity experiments were performed using a Beckman XL-1 analytical ultracentrifuge. Each two-sector sample cell contained 7.5 μM NT13 in one chamber ($A_{280} \approx 1.0$) and sample buffer [50 mM KPO_4 (pH 7.4), 200 mM KCl, and 5% glycerol] in the other as a reference. For complexes containing CO and YC-1, NT13 was diluted into CO-saturated buffer containing 50 μM YC-1 ($A_{330} \approx 1.0$). Spectra were measured pre- and postultracentrifugation to ensure that no protein had been lost to precipitation, and that CO had not been lost during the experiment. Centrifugation was performed at 40000 rpm for 12 h at 4 °C and absorbance measured every 15 min at 280, 330, or 430 nm. Data were fit using SEDFIT[27] with the following parameters calculated by SEDNTERP:[28] buffer density, 1.024 g/cm^3; viscosity, 0.0189 g cm^{-1} s^{-1} (poise).

Chemical Cross-Linking and Protein Digestion. Cross-linking reagents BS^2G [bis(sulfosuccinimidyl)glutarate-d_0], BS3 [bis(sulfosuccinimidyl)suberate-d_0], EDC {1-ethyl-3-[3-(dimethylamino)propyl]carbodiimide hydrochloride], and BMOE [bis-(maleimido)ethane} were purchased from Pierce (Rockford, IL). Sequencing-grade trypsin was purchased from Promega (Madison, WI), and all other chemicals were purchased from Sigma-Aldrich unless otherwise stated. The homobifunctional cross-linking reagents BS^2G and BS3 were prepared individually as stock solutions (50 mM) in DMSO shortly prior to addition and added at a final concentration of 1 mM to samples containing 20 μM *Ms* sGC NT13 or NT19 [in 50 mM potassium phosphate buffer (pH 7.4) and 300 mM KCl]. All final reaction volumes were 50 μL. For the heterobifunctional cross-linker EDC, a stock solution was prepared containing 1 M EDC and 2.5 M NHS (*N*-hydroxylsuccinimide) and was added to a 20 μM *Ms* sGC NT13 sample, leading to final concentrations of 20 mM EDC and 50 mM NHS, and a final volume of 50 μL. The reactions were conducted on ice for 1 h and were quenched by addition of NH_4HCO_3 (20 mM final concentration). Reaction mixtures with BMOE contained 70 μM NT19 and a 6-fold excess of cross-linker, and reactions were conducted for 1 h at room temperature and quenched via the addition of 5 mM DTT. Cross-linked protein samples were visualized on a precast 10% polyacrylamide gel (Bio-Rad) and stained with Coomassie brilliant blue. In-gel trypsin digestion was performed following the Mann protocol.[29]

Mass Spectrometry for Cross-Linked Peptide Identification. An LTQ Orbitrap Velos mass spectrometer (Thermo Fisher Scientific, San Jose, CA) fronted with a Proxeon nanoEasy high-performance liquid chromatography system (Thermo Fisher Scientific) coupled using a NanoMate nanospray source (Advion, Ithaca, NY) was used to analyze the tryptic digests from sodium dodecyl sulfate−polyacrylamide gel electrophoresis (SDS−PAGE). The peptide sample was first loaded on a trap column (100 μm × 2 cm, C-18, Easy column, Thermo Fisher Scientific) with 100% solvent A (0.1% formic acid) at a flow rate determined by maximal 280 bar pressure loading, generally 20 μL/min. The sample was then separated on a nano column (75 μm × 10 cm, C-18, Easy column) using a 50 min gradient from 5% B (0.1% formic acid in acetonitrile) to 35% B, followed by a 5 min gradient to 85% B and then a 5 min gradient to 95% B at a rate of 300 nL/min. The peptides were directly introduced into the LTQ Orbitrap Velos using the NanoMate with the spray voltage set at 1.77 kV. To identify the cross-linked peptides, data-dependent MS/MS analysis (m/z 350−2000) was performed using MS acquisition software (Xcalibur version 2.1, Thermo Fisher Scientific) in which a full high-resolution MS scan at 30000 resolution was followed by a maximum of 10 MS/MS scans of the 10 most intense precursor ions with charge states of ≥4. To perform MS/MS of the less abundant ions, dynamic exclusion was set to select and fragment those ions once and then place the selected ion on an exclusion list for 45 s. Precursor ions were selected and excluded using the monoisotopic precursor selection (MIPS) feature of the LTQ Orbitrap Velos, which allowed a selected ion width of 10 ppm and required that the isotope pattern of the selected precursor fit a model for peptide ions calculated for a similar mass. For MS/MS, precursor ions were selected with a mass width of 4 amu and were fragmented in the ion trap at 50% relative energy with a 30 ms activation time before being transferred to the Orbitrap for mass measurement at 7500 resolution. MS/MS spectra were converted to *.dta files using Thermo Proteome Discoverer version 1.2 (Thermo Fisher Scientific) for de novo sequencing.

MS/MS Data Analysis. Tandem mass spectral data were converted into peak lists (.dta files), deconvoluted, and searched by an in-house program.[30] Briefly, a list of potential peptides from trypsin digest was generated, and masses of linear peptide combinations that included cross-linker masses were searched against the corresponding peak list files. Calculated masses of b- and y-ion fragments were searched against the MS/MS peak list files, and lists of identified matches were scored with respect to the number of fragments identified. Independent verification of each match was achieved by manual comparison of the raw data from Xcalibur (Thermo Fisher) with MS/MS fragment lists from GPMAW (Lighthouse Data) and/or Protein Prospector.[31] Cross-linked peptides were considered reliable if 10 or more fragments were identified, if the calculated and experimental cross-linked peptide masses were agreeable, if fragments that contain the cross-linker and portions of both peptides were observed, and if the same cross-linked peptide was found in multiple scans.

Small-Angle X-ray Scattering and Shape Reconstruction. Small-angle X-ray scattering (SAXS) data were measured at Stanford Synchrotron Radiation Lightsource beamline 4-2. Proteins were confirmed to be monodisperse at concentrations used for SAXS by dynamic light scattering (DLS), using a Wyatt DynaPro NanoStar instrument. DLS size distribution histograms were calculated with DYNAMICS version 6.12 (Wyatt Technology Corp.). Prior to SAXS measurement, *Ms* sGC NT proteins were concentrated using a Vivaspin 50 kDa cutoff filter (Sartorius Stedim Biotech, Goettingen, Germany). During the final concentration step, the proteins were washed with fresh gel filtration buffer three times and the filtrates collected for use in the blank SAXS measurements to ensure the buffer composition of the blank matched that of the sample. SAXS samples were prepared by diluting protein with the blank buffer supplemented with 1 mM fresh TCEP in series from 10 to 1 mg/mL. CO complexes were

prepared by dilution with a buffer saturated with CO gas. NO complexes were prepared by addition of a 100 μM solution of DEA/NO dissolved in 10 mM NaOH. YC-1 and BAY 41-2272 complexes were prepared by addition of a 4 mM solution of YC-1 or BAY 41-2272 in DMSO to the sample before addition of protein. Final DMSO concentrations in each sample never exceeded 2%. Buffer subtraction and data averaging were performed using *SASTOOL*.[32] Molecular masses were calculated using an SSRL program based on the method of Orthaber et al.[33] R_g and $I(s)$ analyses were performed using PRIMUS,[34] and $p(r)$ distribution function analysis was performed using GNOM.[35] Quality scores based upon the Guinier plot were calculated using AutoRg.[36] Ab initio shape reconstruction was performed, both with and without symmetry restraints, using DAMMIN or GASBOR.[37] Averages of ≥10 models were created using DAMAVER.[38] UltraScan[39] was used to calculate the sedimentation coefficient and Stokes radius for the bead model shape reconstructions computed from the SAXS envelopes. CRYSOL[40] was used for comparing model and experimental scattering curves. Molecular envelopes were displayed using Chimera.[41]

Homology Modeling. Homology models of individual domains were generated using the bioinfobank meta server.[42] After domain modeling, 20% of the protein remained unmodeled. To obtain models for this region, the sequence was submitted to the Robetta server (http://robetta.bakerlab.org).[43] For the individual domains, the models generated with Robetta were similar to those generated through homology modeling. In regions outside the domains, if the secondary structure was predicted to be helical or β sheet, residues in those regions were constrained to adopt that conformation. Homology models were displayed with either Chimera[41] or PyMol (DeLano Scientific, San Carlos, CA, http://www.pymol.org/).

Model Assembly. The *Ms* sGC NT19 model was built in an incremental fashion. First, the conformation of the coiled coil was determined, and the β_1 H-NOX, α_1 PAS, α_1 H-NOX, and β_1 PAS domains were then incrementally added. In each step, candidate interfaces between the two components were generated using ZDOCK.[44] The rotational sampling was set to be dense ($-D$ parameter), and 50000 conformations were generated for each dock run. The conformations that satisfied the cross-linking restraints were selected, and one of those was taken forward for adding the remaining components. Finally, the model was refined using molecular dynamics in a structure-based force field[45] with two biasing forces derived from the SAXS envelope and the cross-linking restraints. The former biasing force was employed using the flexible fitting program MDfit,[46,47] as used previously in a cryo-electron microscopy fitting study.[48] MDfit is based on Gromacs[49] and allowed us to simultaneously incorporate the later biasing of cross-linking restraints, which were modeled as distance restraints in Gromacs with a force constant of 1000 kJ mol^{-1} nm^{-2}.

The docking process started by identifying the coiled-coil conformation, because most cross-links included residues in this region. Among the 50000 coiled-coil conformations generated using ZDOCK, many satisfied the cross-linking restraints. To select the best model based on the interaction energies, rescoring was performed using ZRANK[50] and the top 1000 conformations were selected; only 86 of those conformations were found to be consistent with the cross-linking restraints. These conformations were then clustered into 10 bins based on the root-mean-square deviation. The top-ranked model, which also belongs to the largest cluster, was then selected for docking with the β_1 H-NOX domain. Docking of the coiled coil with the β_1 H-NOX domain resulted in a single cluster (~40 conformations among the 50000 generated) that satisfied all four cross-linking restraints, and the lowest-energy conformer among these was chosen. The coiled-coil–β_1 H-NOX domain model was then docked with α_1 PAS and α_1 H-NOX domains, separately. Both dockings resulted in multiple candidate orientations that satisfied the cross-linking restraints, 4 and 50 candidates for the α_1 PAS and α_1 H-NOX domains, respectively. These candidates were then combined in all possible combinations (200), and conformations with steric clashes between the α_1 PAS and α_1 H-NOX domains were removed, leading to 36 models containing the coiled-coil, α_1 H-NOX, β_1 H-NOX, and α_1 PAS domains. Further consideration of chain connectivity, cross-linking restraints, and SAXS envelope fitting using the refinement procedure described above identified four potential models. The fittings of the models into the SAXS envelope were visually inspected, and the most promising model was selected. To obtain the final *Ms* sGC NT19 model, the β_1 PAS domain was initially intuitively added to the most promising model, because of the lack of cross-linking restraints, and the new model was refined using the protocol described above. The final model satisfies all of the experimental restraints and fits well in the SAXS envelope but does not include residues α_1 267–279 or β_1 183–194, which link the H-NOX and PAS domains, or residues α_1 391–406 and β_1 317–336, which link the PAS and coiled-coil domains, because reliable models for these regions were unavailable. Also missing are the six-His and *Strep* purification tags.

CO Binding Affinity. CO dissociation constants for *Ms* sGC NT constructs were measured using a previously published procedure.[24] The *Ms* sGC NT protein samples were prepared at a concentration of 1 μM in 50 mM KPO_4 (pH 7.4), 100 mM KCl, and 5% glycerol and placed in a septum-capped cuvette at room temperature (~22 °C). Buffer saturated with CO gas was assumed to contain 1 mM CO, based on the CO solubility in water at room temperature.[51] Aliquots from CO-saturated buffer were added to the cuvette and mixed, and the spectrum was measured. When present, YC-1 (50 μM) or BAY 41-2272 (5–10 μM) was added before addition of CO. Binding of CO to heme was measured by the shift in unliganded Soret absorbance (430–434 nm) to that of the CO complex (423–424 nm) after accounting for dilution because of the addition of CO. Data were fit to a single-site saturation ligand binding model using SigmaPlot (SPSS, Inc., Chicago, IL).

Proximal Histidine Release Rates upon Binding of NO to Heme. The rates for release of β_1 His-105 upon binding of NO to *Ms* sGC NT1, -2, -13, -19, and -21 were measured at 10 °C by mixing 1 μM protein and 10 μM NO in an RSM-1000 stopped-flow spectrophotometer (OLIS, Inc.), using a previously published procedure.[24] Protein samples were prepared by deoxygenating buffer through bubbling of argon gas for at least 20 min, followed by addition of protein in a gastight syringe, and transfer to the stopped-flow device. NO solutions were prepared by addition of DEA/NO from a stock solution to argon-purged buffer in a gastight syringe and then connected to the stopped-flow device. DEA/NO decomposition was allowed to proceed for 20 min at room temperature before the sample was transferred to the instrument, where the solution was allowed to equilibrate to the desired temperature (5 min). Absorbance changes (A_{420}) were fit to single- or double-exponential equations using SigmaPlot; values reported are the average and standard deviation of three to five consecutive measurements.

RESULTS

Development of Truncated sGC Proteins for Functional Analyses. Functional studies of sGC are impeded by

dx.doi.org/10.1021/bi301570m | *Biochemistry* XXXX, XXX, XXX–XXX

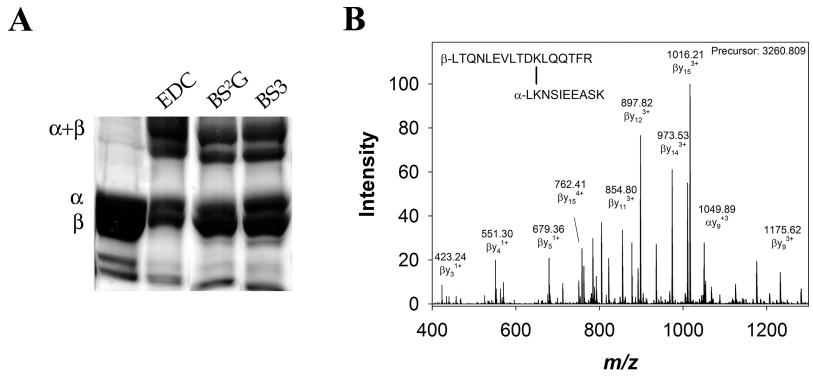

Figure 2. Representative cross-linking results. (A) Cross-linked *Ms* sGC NT13, examined by SDS−PAGE and stained with Coomassie brilliant blue. Individual bands were cut from the gel, digested with trypsin, and examined by tandem mass spectrometry. (B) Representative cross-linked peptide MS/MS spectrum. The BS^2G α_1 K434−β_1 K366 cross-link was found in the +4 charge state because of two amine termini and lysine/arginine at the trypsin cleavage sites and displayed a 22 ppm error in observed vs calculated precursor mass (Table 1). The cross-linked peptide was observed and selected for fragmentation in seven scans in a single experiment. Between 7 and 36 fragments were identified in each scan, each with a mass accuracy of approximately 1 ppm. Representative fragments are labeled in the mass spectrum. Identified fragments in this spectrum included β_1 fragments b_4−b_{10}, y_2−y_6, and y_8−y_{15} (which contain the cross-linker and entire α_1 peptide), α_1 fragments y_2−y_8, and α_1 fragments b_3−b_5 (which contain the cross-linker and entire β_1 peptide).

Table 1. α_1/β_1 Intermolecular Cross-Links

cross-linker	α_1 peptide	residue	β_1 peptide	residue	precursor mass (MH+)	error (ppm)
BS^2G (7.7 Å)	92−101	K98	356−372	K366	3343.808	16
	254−273	K255	28−40	K28	3585.800	23
	254−273	K255	356−372	K366	4211.143	7
	430−434	K432	1−26	K15	3899.969	12
	429−434	K432	356−372	K366	2932.624	11
	433−442	K434	342−366	K366	4156.138	12
	433−442	K434	356−372	K366	3260.809	22
	435−448	K442	356−372	K366	3717.969	11
	443−448	K446	356−372	K366	2859.543	8
BS3 (11.4 Å)	92−101	K98	373−380	K378	2413.274	4
	340−344	K343	169−188	K170	3090.564	3
	430−434	K432	356−372	K366	2818.544	2
	429−434	K432	356−372	K366	2974.649	0
	429−442	K432	356−372	K366	3833.035	6
	430−434	K432	373−380	K378	1787.979	7
	429−434	K432	373−380	K378	1944.078	8
	429−442	K432	373−380	K366	2802.469	12
	433−442	K434	356−372	K366	3302.785	3
	433−442	K434	373−380	K380	2272.224	6
	435−446	K442	356−372	K366	3474.920	25
	435−448	K442	373−380	K378	2729.413	6
	443−448	K446	356−372	K366	2901.578	0
	435−448	K446	356−372	K366	3759.980	2
	443−448	K446	373−380	K380	1871.003	10
	449−Strep9	K450	373−380	K378	2570.316	3
	449−Strep9	Strep-K9	356−372	K366	3600.876	1
	Strep1−9	Strep-K9	356−372	K366	3343.730	4
	Strep1−9	Strep-K9	373−380	K378	2313.175	5
EDC (0 Å)	254−273	E256	28−40	K28	3529.734	12
	277−293	K286	189−207	E196	4087.173	15
	340−344	E340	169−188	K170	2934.515	5
	355−368	E366	373−380	K378	2414.309	10
	412−421	E418	73−95	K85	3714.971	27
	443−448	K446	16−27	E20	3083.537	6

difficulty with obtaining robust material. We have developed sGC from *M. sexta* (*Ms* sGC) as a model system and have produced truncated recombinant heterodimeric proteins in sufficient quantity and purity for biophysical studies.[24,26] For these studies, we employed sGC truncations lacking the C-terminal regions of both subunits, including the catalytic domains, and portions of the N-terminal region of the α_1 subunit (Figure 1). The truncated proteins have ferrous heme, display

dx.doi.org/10.1021/bi301570m | *Biochemistry* XXXX, XXX, XXX−XXX

Table 2. Intramolecular Cross-Links

α_1 Intramolecular Cross-Links						
cross-linker	α_1 peptide	residue	α_1 peptide	residue	precursor mass (MH+)	error (ppm)
BS^2G (7.7 Å)	115−127	K122	196−220	K216	4217.293	12
	217−221	K220	241−255	K253	2483.419	12
	254−273	K255	287−297	K296	3580.778	18
BS3 (11.4 Å)	115−127	K122	196−220	K216	4259.298	5
	123−142	K127	217−221	K220	3097.607	9
	217−221	K220	254−273	K253	2222.257	8
	217−221	K220	241−255	K253	2525.432	5
	217−221	K220	254−273	K255	2821.421	3
	254−273	K255	287−297	K296	3680.792	4
	254−273	K255	428−434	K432	3225.611	6
	287−297	K296	340−344	K343	2213.222	5
	430−434	K432	435−448	K442	2347.212	7
	429−434	K432	443−448	K446	1644.908	8
	430−434	K432	449−Strep9	K450	2188.110	5
	430−434	K432	Strep1−9	Strep-K9	1930.970	7
	429−434	K432	Strep1−9	Strep-K9	2087.076	4
	433−442	K434	443−448	K446	1973.044	11
	433−442	K434	449−Strep9	K450	2672.359	3
	435−446	K442	449−Strep9	K450	2844.400	5
	435−448	K442	449−Strep9	K450	3129.544	5
	443−448	K446	449−Strep9	K450	2271.136	6
EDC (0 Å)	243−253	K253	254−273	E256	3418.716	18
	243−253	K253	254−273	E264	3418.744	26
β_1 Intramolecular Cross-Links						
cross-linker	β_1 peptide	residue	β_1 peptide	residue	precursor mass (MH+)	error (ppm)
BS^2G (7.7 Å)	1−26	K15	152−163	K156	4592.254	10
	373−380	K378	356−372	K366	3158.749	17
BS3 (11.4 Å)	356−372	K366	373−380	K380	3200.742	3

CO and NO binding characteristics similar to that of the full-length enzyme, and retain binding of the allosteric stimulators YC-1 and BAY 41-2272.[24] Construct NT2[24] contains the H-NOX, PAS, and coiled-coil domains of *Ms* sGC α_1 and β_1 (α_1 49−471, β_1 1−401), while truncation of ∼20 residues from the C-termini of both subunits leads to the more stable construct NT13 (α_1 49−450, β_1 1−380).[26] For SAXS experiments, which require high purity and monodispersity at high concentrations, we developed construct NT19, which contains an additional streptavidin purification tag (WSHPQFEK). The additional purification step led to a protein with an extremely high purity that was monodisperse at concentrations up to 8 mg/mL as estimated by dynamic light scattering (see below). We also prepared protein NT21, which lacks the α_1 H-NOX domain, to investigate the role of this domain and to help in the identification of the domain arrangement in the protein. This protein was also prepared in high purity and was monodisperse at high concentrations.

As with NT2 and NT13,[24,26] NT19 and NT21 were heterodimeric and displayed typical Soret maxima for unliganded (433 nm), NO-liganded (400 nm), and CO-liganded (423 nm) complexes. The A_{432}/A_{280} ratio was 1.6:1 and 1.9:1 for NT19 and NT21, respectively, indicating a high level, likely complete, of heme incorporation. CO binding was slightly tighter to NT21 than to NT19 or NT2 (Figure 1). Interestingly, NT21 still responds to YC-1 (Figure 1), indicating YC-1 does not bind to the α_1 H-NOX domain.

Chemical Cross-Linking and Mass Spectrometry. We undertook chemical cross-linking coupled with high-resolution mass spectrometry to determine close contacts between sGC domains. Such methods can provide powerful restraints for model building.[52] We chose the readily available amine-reactive cross-linkers BS^2G and BS3, and the amine carboxyl-reactive cross-linker EDC for these studies. The succinimidyl esters of BS^2G and BS3 react with two nearby lysine residues, providing covalent attachments that can later be identified by mass spectrometry. The carbon spacer arms between the reactive groups differ in length (7.7 Å for BS^2G and 11.4 Å for BS3), allowing for the capture of lysines separated by differing distances. The EDC cross-linker is zero-length; one end reacts with free carboxyl groups of aspartate or glutamate and the other with nearby lysine side chains, leading to a peptide bond between the two amino acids. It is therefore useful for detecting intermolecular salt bridges.

Both *Ms* sGC NT13 and *Ms* sGC NT19 proved to be amenable to cross-linking. These constructs differ by the presence of a C-terminal Strep tag on the α subunit of NT19. Covalently linked $\alpha_1\beta_1$ subunits were readily identified on denaturing polyacrylamide gels (Figure 2A), allowing for the bands to be cut out and subjected to in-gel trypsin digestion, followed by mass spectrometry (Figure 2B). The peptides were analyzed on a hybrid linear ion trap-Orbitrap instrument, and high-charge state peptides (at least +4) were selected for collision-induced dissociation (CID) fragmentation. The observed precursor and fragment masses were matched to masses of predicted peptides. Tables 1 and 2 list the 34 intermolecular and 26 intramolecular cross-linked peptides identified for NT13 and NT19, respectively; a representative MS/MS spectrum and fragment assignment is displayed in Figure 2B. A cysteine-reactive maleimide cross-linker (BMOE, 8 Å)

dx.doi.org/10.1021/bi301570m | *Biochemistry* XXXX, XXX, XXX−XXX

also successfully cross-linked α_1 and β_1 subunits; however, no cross-linked peptides were identified by our search methods.

The high mass accuracy of precursor and fragment peptides provided confidence in the assignments; mass errors for cross-linked peptides were generally less than 0.1 amu (Tables 1 and 2), and mass errors for fragment peptides were ~1 ppm. Cross-linked peptides were considered reliable if ≥10 fragments were identified, the calculated and experimental peptide masses were agreeable, and fragments that contained the cross-linker and portions of both peptides were observed. Additionally, many cross-links were identified in both BS^2G and BS3 cross-linking experiments, and in both the NT13 and NT19 experiments, highlighting the reproducibility of our methods.

A summary of the intermolecular cross-links and restraints used in model building can be found in Table 3 and is shown graphically in Figures 3 and 4. It is clear from the extensive cross-links between residues in the predicted coiled-coil region that the coiled coil likely does form and, furthermore, has parallel $\alpha_1\beta_1$ strands (Figure 3). Sixteen unique cross-linked peptides were found within the $\alpha_1\beta_1$ coiled coil, which spans residues α_1 419–450 and β_1 355–380; an additional cross-link was found in NT19 between β_1 Lys-380 and Lys-9 of the C-terminal α_1 Strep tag. Most of these cross-links are consistent with only a parallel coiled-coil model (Figure 3). In particular, cross-links formed between α_1 442 and β_1 378, α_1 446 and β_1 380, α_1 450 and β_1 378, and α_1 Strep tag 9 and β_1 380 are 42–49 Å apart in the antiparallel model, distances far greater than the 23 Å maximal Cα–Cα distance that can be spanned by the BS3 linker. In contrast, the maximal Cα–Cα distance spanned by linkers is 16 Å for the parallel model. This agrees with the conclusions of Ma and co-workers, who preferred a parallel coiled-coil arrangement based on electrostatic arguments despite the crystal structure of the rat sGC β-homodimer containing an antiparallel coiled coil.[23]

Nine cross-links were found between the coiled-coil and other domains in *Ms* sGC NT proteins; eight of these were between the α_1 and β_1 strands. Five additional cross-links were found between the other domains, four of which were between α_1 and β_1 subunits. Taken together, these data suggest major interdomain contacts between subunits on opposite chains. In particular, the α_1 PAS domain appears to be closely associated with the β_1 H-NOX domain, which, in turn, is closely associated with the α_1 coiled coil.

Table 3. Summary of Chemical Cross-Links and Modeling Distance Restraints

α_1 residue	domain	β_1 residue	domain	distance (Å)
K98	H-NOX	K366	coiled-coil	21
K98	H-NOX	K378	coiled-coil	25
K255	H-NOX	K28	H-NOX	21
K255	H-NOX	K366	coiled-coil	21
E256	H-NOX	K28	H-NOX	13
K286	PAS	E196	PAS	13
E340	PAS	K170	H-NOX	13
K343	PAS	K170	H-NOX	25
E366	PAS	K378	coiled-coil	13
E418	coiled-coil	K85	H-NOX	13
K432	coiled-coil	K15	H-NOX	21
K432	coiled-coil	K366	coiled-coil	21
K432	coiled-coil	K378	coiled-coil	25
K434	coiled-coil	K366	coiled-coil	21
K434	coiled-coil	K380	coiled-coil	25
K442	coiled-coil	K366	coiled-coil	21
K442	coiled-coil	K378	coiled-coil	25
K446	coiled-coil	E20	H-NOX	13
K446	coiled-coil	K366	coiled-coil	21
K450	coiled-coil	K378	coiled-coil	25

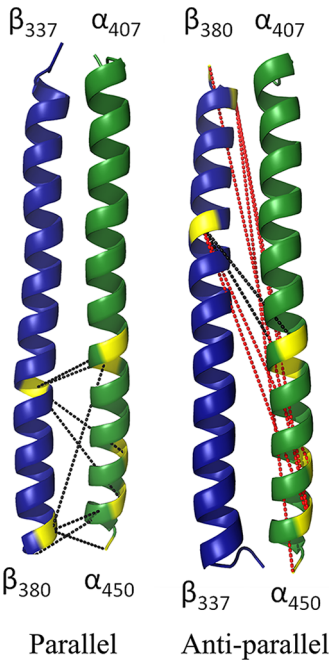

Figure 3. Cross-links within the *Ms* sGC coiled coil. Displayed are homology models built for the *Ms* sGC α_1/β_1 coiled coil in both parallel and antiparallel orientations. Colored yellow are lysine residues found cross-linked with BS^2G or BS3 (7.7 or 11.4 Å spacer arm, respectively). Black dashes indicate Cα distances in the model between 6 and 19 Å, appropriate for cross-linking; red dashes indicate distances between 30 and 48 Å, unlikely to be found in cross-links. These data confirm a parallel coiled-coil arrangement in sGC.

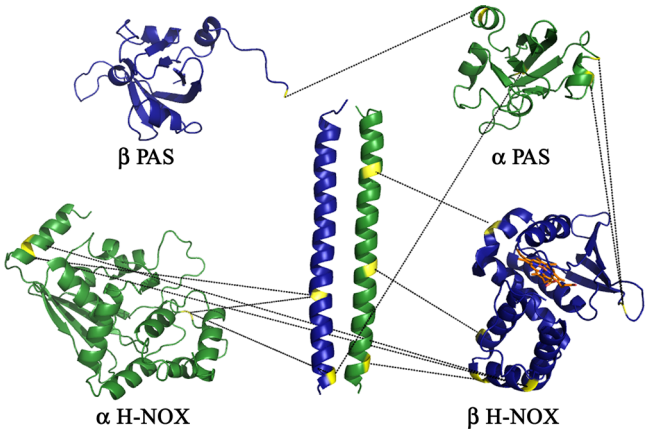

Figure 4. Expanded diagram of intermolecular cross-links between *Ms* sGC α_1 and β_1 subunits. Displayed are homology models of each *Ms* sGC domain, with residues found in BS^2G, BS3, or EDC cross-links colored yellow and connected by black dashes. Cross-links within the coiled coil have been omitted for the sake of clarity.

Analytical Ultracentrifugation Indicates sGC Is Elongated. Little is known about the general shape of sGC or how it changes in response to allosteric effectors. We employed sedimentation velocity analytical ultracentrifugation, which is sensitive to molecular shape, to begin investigating these

dx.doi.org/10.1021/bi301570m | *Biochemistry* XXXX, XXX, XXX–XXX

properties in *Ms* sGC NT13 and NT21. Each protein sedimented as a single species during the long (~12 h) runs and yielded a calculated molecular mass generally within 5% of the actual value (Table 4).

Table 4. Biophysical Parameters Determined by Analytical Ultracentrifugation[a]

complex	S	S(20,w)	molecular mass (kDa)	frictional ratio (f/f_0)	Stokes radius (Å)
NT13	2.6 ± 0.10	5.5	87	1.3	38
NT13 with YC-1	2.4 ± 0.12	5.0	91	1.5	43
NT13 with CO and YC-1	2.4 ± 0.08	5.0	86	1.4	40
NT13 SAXS bead model	2.4	–	–	1.3	38
NT21	2.2 ± 0.02	4.5	64	1.3	34
NT21 with CO and YC-1	2.0 ± 0.03	4.0	66	1.5	39

[a]Displayed are the sedimentation coefficient (S) values under experimental conditions and extrapolated to 20 °C in H_2O [S(20,w)] and the molecular masses, frictional ratios, and Stokes radii all computed from the sedimentation coefficient distribution. Each value reported is the average of a single sample measured at multiple wavelengths (400−432 nm for heme Soret, 280 nm for protein backbone, and 330 nm for YC-1, when present). The error in S is reported as the standard deviation from $c(S)$ distribution peak integration. The error between the raw data and the Lamm equation fit was small in all cases (between 0.009 and 0.015) and is not reported. Each sedimentation velocity experiment was conducted two or three times, and the results correlate well (not shown). Hydrodynamic parameters computed from UltraScan for a molecular envelope for NT13 are consistent with the size measured via ultracentrifugation (not shown). The calculated molecular masses correlate well for both NT13 and NT21 (90.3 and 65.0 kDa, respectively). Data measured in the presence of NO behaved badly and are not included (see the text).

Sedimentation was followed by absorption of the heme Soret band (400−432 nm, depending on the complex), the protein (280 nm), or compound YC-1, when present (330 nm). Analysis of the data acquired for each wavelength yielded the same sedimentation coefficients and frictional ratios. Unliganded *Ms* sGC NT13 displayed a sedimentation coefficient (S) of 2.6 and a frictional ratio (f/f_0) of 1.3 (Table 4), indicative of an elongated molecule (a spherical molecule would have an f/f_0 of 1). A similar value (f/f_0 = 1.35) was obtained from models derived from SAXS experiments (described below). Sedimentation of *Ms* sGC NT21, which has the entire α_1 H-NOX domain removed (~25 kDa), followed the same trend as that of NT13 (Table 4). It too behaved as an elongated molecule and has the same frictional ratio as NT13. Binding of both CO and YC-1 led to an increase in the frictional ratio. Thus, the α_1 H-NOX domain appears not to have a functional role in YC-1 binding.

The sedimentation velocity data for the NO complexes fit well only when the molecular mass of the protein is significantly underestimated; hence, we consider these results unreliable, and they have not been included in Table 4. It may be that some denaturing or dissociation of the protein occurs during the several hours of the sedimentation experiment. Similar problems did not occur in the small-angle scattering experiments (see below), which were conducted on a much shorter time scale (minutes vs hours between sample preparation and the end of data collection).

Small-Angle X-ray Scattering. After confirming that the protein constructs were monomeric in solution by gel filtration, analytical ultracentrifugation, and dynamic light scattering (Figure 5A,B), we performed small-angle X-ray scattering experiments to determine molecular envelopes for *Ms* sGC NT constructs and to uncover any large structural changes that might occur upon ligand binding. In SAXS experiments, two parameters can be determined from the scattering curves. First, the radius of gyration (R_g) of the molecule is extracted from the linear relationship between scattering intensity $I(s)$ and angle (s^2, Å^{-2}) at low scattering angles.[53,54] Second, D_{max}, the maximal radial distance, is extracted from the distribution function, $p(r)$, which is determined by Fourier transform of the scattering intensity and is a representation of the distribution of radial distances throughout the macromolecule.[53,54] We performed SAXS measurements for *Ms* sGC constructs NT2, NT13, NT19, and NT21 (Table 4). Of these, NT19 and NT21 had the highest purity and weakest tendency to aggregate at high concentrations and yielded the best scattering curves. Both NT19 and NT21 had a slight increase in R_g at concentrations of >5 mg/mL, indicating a slight attractive interaction. For both NT19 and NT21, the molecular mass estimated from $I(0)$ is within 5% of the actual value.

Unliganded NT19 has an R_g of 34 Å and a D_{max} of 115 Å. The molecule is elongated, and the calculated frictional ratio (f/f_0 = 1.35) agrees with that obtained from ultracentrifugation experiments. Surprisingly, unliganded NT21, which lacks the α_1 H-NOX domain, displayed nearly the same R_g and D_{max} values as NT19, despite the loss of the 25 kDa domain. Addition of NO or CO and BAY 41-2272, or CO and YC-1, had little effect on the scattering profiles or derived quantities for either NT19 or NT21 (Figure 5), indicating that overall shape changes upon YC-1 binding, or NO binding and proximal histidine release, are small. Examination of SAXS intensity decay as a function of scattering angle (Kratky plot), which is sensitive to protein disorder,[55] indicates that NT19 and NT21 are well-folded but display some flexibility. Ligand addition had little effect on scattering decay.

Ab initio methods have been developed for the reconstruction of low-resolution molecular envelopes for protein molecules using SAXS data. We determined molecular envelopes for NT19 and NT21 using DAMMIN,[37] which calculates an arrangement of dummy atoms whose computed scattering profile is minimized against that of the experimental SAXS data.[37] Final envelopes were the average of at least 10 starting envelopes, calculated using DAMAVER.[38] For NT19, the computed molecular envelope has a volume of 178 × 10^3 Å^3, an appropriate size for two H-NOX and two PAS domains. NT21 has a similar envelope that is narrower at one end and has a calculated volume of 135 × 10^3 Å^3, a difference of 43 × 10^3 Å^3, an appropriate difference in volume for a molecule lacking one H-NOX domain. The differing envelope shapes in conjunction with the chemical cross-linking results described above provide guidance for model building (Figure 6).

The α_1 and β_1 subunits of sGC arise from gene duplication, suggesting the overall molecular structure may display 2-fold pseudosymmetry. However, imposing $P2$ symmetry in DAMMIN resulted in a significantly poorer χ^2 for the fit to the scattering curve, indicating that the *Ms* sGC NT constructs are not highly symmetric. As a further check on the reliability of the reconstruction, we calculated the predicted hydrodynamic properties of the NT13 bead model, using UltraScan,[39] for comparison with the sedimentation experiments. The predicted values were in good agreement with those measured by ultracentrifugation (Table 4).

Molecular Modeling. Homology models of the *Ms* sGC α_1 and β_1 H-NOX, PAS, and coiled-coil domains were built using Modeler,[56] as previously described.[24] These models are based on structures of related bacterial H-NOX proteins [Protein Data

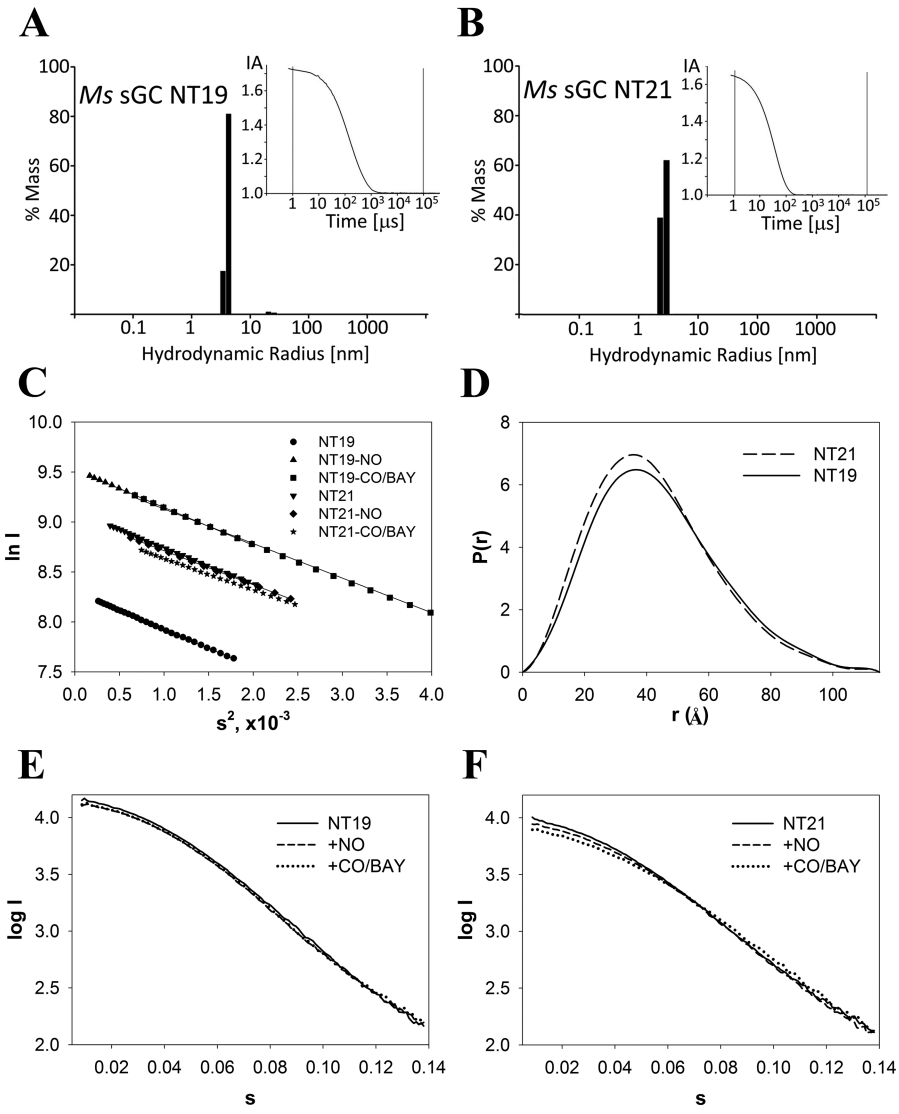

Figure 5. Representative DLS and SAXS data. DLS size distribution histograms are shown for *Ms* sGC NT19 (A) and *Ms* sGC NT21 (B) (2 mg/mL each). The histograms were derived from a regularization analysis of the autocorrelation curve (insets). The intensity autocorrelation (IA) was evaluated as a function of time delay between 1 μs and 0.1 s. *Ms* sGC NT19 displays 8.0% polydispersity, while NT21 displays 9.6% polydispersity. (C) Guinier plots for all NT19 and NT21 complexes, computed from merged data sets (1.3 and 5.0 mg/mL for the small-angle and large-angle data, respectively). (D) Overlay of the NT19 and NT21 pair distance distribution functions $p(r)$, computed using GNOM. (E) Overlay of scattering curves for NT19, NT19 with NO, and NT19 with CO and BAY 41-2272. The curves show very little difference in scattering intensity distribution, indicating little change in shape upon complex formation. (F) Similar overlay for NT21 complexes (uncorrected), which also indicate little change in scattering intensity upon complex formation.

Bank (PDB) entry 2O09],[21] PAS proteins (PDB entries 2P04 and 2P08),[22] and the recent rat β coiled-coil homodimer (PDB entry 3HLS).[23] Several intramolecular cross-links were found within domains that were consistent with the homology models, including β_1 K15–β_1 K156 (β_1 H-NOX domain), α_1 K122–α_1 K216, and α_1 K127–α_1 K220 (α H-NOX domain) cross-links. No intramolecular cross-links were found that were inconsistent with the homology models. Intervening sequences connecting these domains were built using the Robetta server.[43] We considered the Robetta-built domain linker regions to be unreliable, except where helices are predicted to exist.

The domain homology models are expected to have the correct overall folds; however, their arrangement in space is completely unknown. We used a combination of surface matching, cross-link restraints, and fitting to the SAXS molecular envelopes to obtain three-dimensional models of *Ms* sGC NT19.

Because most cross-links included residues in the predicted coiled-coil region, we began by modeling coiled-coil arrangements. In the crystal structure of the rat β_1 coil, a homodimeric antiparallel coiled coil was found. Nonetheless, the authors concluded that the heterodimeric $\alpha_1\beta_1$ protein is likely parallel, based on sequence matching.[23] We examined surface complementarity using ZDOCK[44] and found both parallel and antiparallel arrangements were possible. However, as noted above, only a parallel coiled-coil arrangement is consistent with our cross-linking data (Figure 3).

To add other domains to the model, we generated starting models using ZDOCK,[44] culling those that were inconsistent with chain connectivity or obviously in conflict with the cross-linking data, and then using a course-grained flexible-fitting molecular dynamics approach for minimizing deviations from the cross-linking results (Figure 6) while also maximizing

dx.doi.org/10.1021/bi301570m | *Biochemistry* XXXX, XXX, XXX–XXX

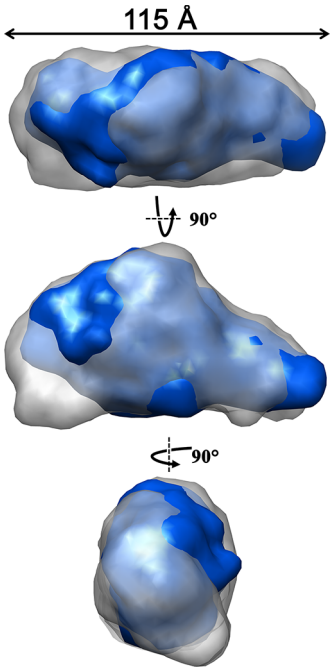

Figure 6. Overlay of DAMMIN reconstructions for NT19 (gray) and NT21 (blue). NT21, which lacks the α H-NOX domain, has a significant volume (~25%) missing from the envelope, although it retains the same D_{max}. The straight arrow indicates the maximal length measurement derived from the SAXS analysis. Displayed with Chimera.

agreement with the molecular envelope generated by SAXS. Docking of the β_1 H-NOX domain was the most robust in this approach, followed by the α_1 PAS domain. Two hundred starting models were initially generated for the coiled-coil, H-NOX, and α_1 PAS domains, a number that was reduced to 36 models based on geometry considerations and further reduced to 4 models based on the flexible fitting refinement. These 4 were all similar in domain placement, differing only in the rotational positioning of the domains. One of these was taken forward for inclusion of the β_1 PAS domain, which was the least constrained (one cross-link and chain connectivity).

The final model fits well with the SAXS molecular envelope (Figure 7). Comparison of the experimental and calculated scattering curves yields a χ of 5.6, a reasonable value considering that domain linkers (~10% of the model) and solvent are missing, the individual domains are based on homology modeling, and the model is fit to the SAXS envelope, not directly to the scattering curve. The most reliable region of the model is the placement of the β_1 H-NOX domain near the center of the parallel coiled-coil region, mostly in contact with the α_1 coiled-coil strand. A slight curve was introduced into the coiled coil during the flexible fitting to the SAXS envelope, around the β_1 H-NOX domain. The α_1 PAS domain lies close to both the β_1 H-NOX domain and the C-termini of the coiled-coil region. This arrangement of the β_1 H-NOX domain near the α_1 PAS domain, organized onto the parallel coiled coil near where the cyclase domains are connected, is likely to provide the heart of the signaling system, as discussed below.

The placement of the remaining two domains is less reliable but allows for two general observations. First, the positions of the α_1 H-NOX and β_1 PAS domains do not appear to mirror those for β_1 H-NOX and α_1 PAS domains and do not appear to be organized on the coiled coil in the same way. Second, the α_1 H-NOX domain is positioned such that its removal would not overly change the shape of *Ms* sGC, as expected from the SAXS and analytical ultracentrifugation experiments (Figure 5), or greatly alter β_1 H-NOX domain activity, as expected from the CO binding experiments (Figure 1).

Stopped-Flow Kinetic Measurements of β_1 His-105 Release upon NO Binding. sGC initially forms a transient six-coordinate intermediate upon binding NO followed by release of the proximal histidine (β_1 His-105), yielding a five-coordinate nitrosyl heme. Each of these is readily detected by absorption spectroscopically because of their distinct Soret absorption maxima, which occur at 433, 420, and 400 nm for the unliganded, six-coordinate, and five-coordinate species, respectively. We previously showed that the six-coordinate intermediate persists sufficiently in *Ms* sGC NT1 for characterization by stopped-flow spectroscopy, yielding a histidine dissociation rate of 12.8 s^{-1}.[24] We examined NO-dependent proximal histidine release for the other NT constructs used in this study and, surprisingly, found that constructs NT13, NT19, and NT21, all of which are shortened with respect to NT1 and NT2 by 21 residues on the α_1 subunit and 20 residues on the β_1 subunit, have greatly increased proximal histidine release rates. In all three cases, release was faster than could be measured in our stopped-flow device (Table 6). Additionally, the truncations in NT13 and NT19 lead to an ~2-fold lower CO dissociation constant in the absence of YC-1 (Figure 1), and truncation combined with removal of the α_1 H-NOX domain in NT21 led to a decrease in CO affinity of nearly 8-fold. The C-terminal truncations are near the end of the predicted coiled-coil region and close to where the β_1 H-NOX domain lies in our model, suggesting these residues are in direct contact with the β_1 H-NOX domain and have a packing arrangement that holds the heme domain in a more open conformation (discussed below).

DISCUSSION

We have produced a molecular model of truncated sGC from *M. sexta*, the first such model for any sGC. We obtained the overall shape of the molecule from SAXS and sedimentation velocity measurements and determined points of domain contact through chemical cross-linking and tandem mass spectrometry. We arranged homology-modeled H-NOX, PAS, and coiled-coil domains into the molecular envelope using flexible fitting and cross-linking constraints. The model that emerges from our studies is one in which sGC is an elongated molecule with functional domains organized around a central parallel coiled-coil segment. A key region near the C-terminus of the coiled coil brings together the β_1 H-NOX, α_1 PAS, and cyclase domains. This arrangement suggests a model for allostery in which domains inhibit one another through direct contact in a manner that can be overcome by binding of ligand to any one of the domains. We discuss the rationale for this model and functional implications in what follows.

Overall Shape and Ligand-Induced Conformational Changes in sGC. Prior to these studies, no information was available concerning the overall shape for sGC or how this shape changes during activation. We have shown, using SAXS and SV-AUC, that a truncated heterodimeric sGC containing approximately two-thirds of the protein but lacking the cyclase domains is an elongated molecule with dimensions of approximately 115 Å × 90 Å × 75 Å. Removal of the α_1 H-NOX domain creates a molecule of roughly the same length but one that is somewhat thinner at one end (Tables 4 and 5 and Figure 6).

sGC is an allosteric protein in which the binding of NO or YC-1 family compounds leads to cyclase activation,[18,57] while

dx.doi.org/10.1021/bi301570m | *Biochemistry* XXXX, XXX, XXX−XXX

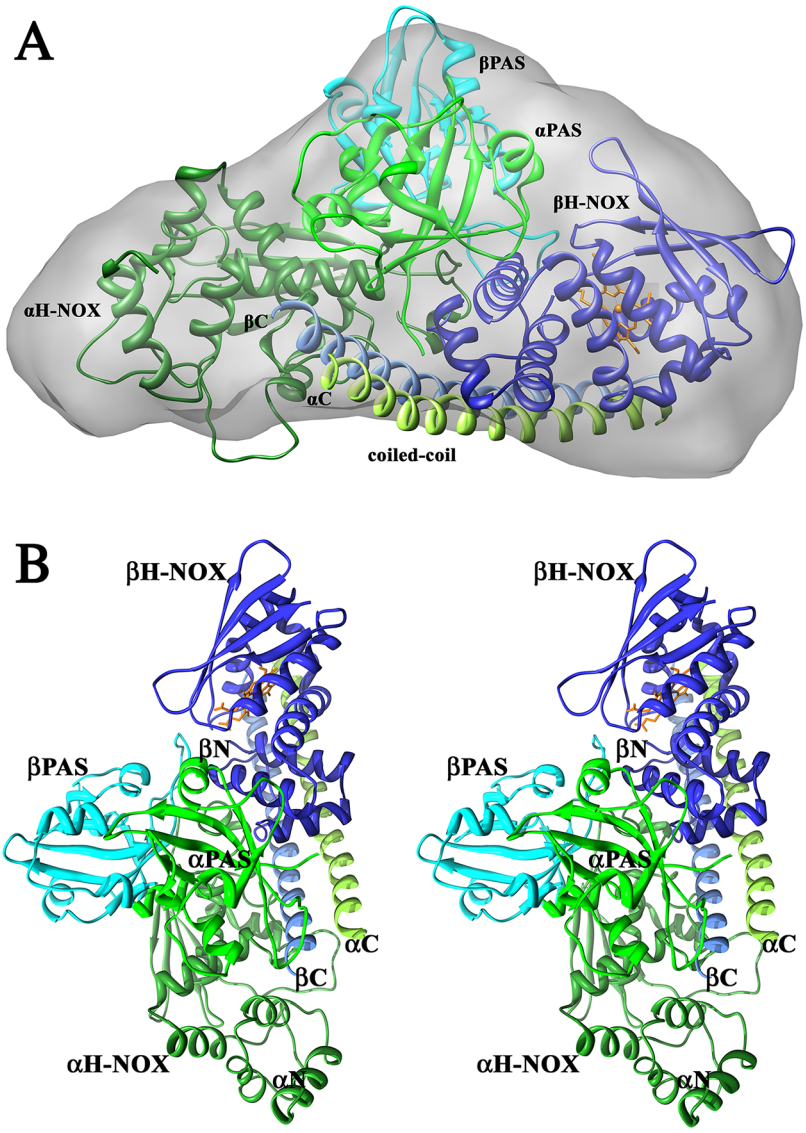

Figure 7. *Ms* sGC model. (A) Restrained model for *Ms* sGC NT19 fit to the SAXS molecular envelope. (B) Stereoview of the restrained model. The α_1 subunit is colored green and the β_1 subunit blue. The N- and C- termini and all domains are labeled. Linker regions between individual domains are not included in the model (α_1 267−279, α_1 391−406, β_1 183−194, and β_1 317−336).

modifications such as phosphorylation lead to cyclase inhibition.[58−60] Likewise, binding of a nucleotide to the cyclase domains can alter the binding of NO to the sGC heme.[61−63] The truncated proteins used in this study retain their allosteric response to YC-1, which, on binding, leads to higher affinities and reduced off rates for CO and NO (refs 24 and 25 and Figure 1). To probe the nature of the conformational changes associated with allosteric response, we undertook SAXS and SV-AUC measurements in the absence and presence of allosteric compounds. For the SAXS measurements, the *Ms* sGC NT proteins were monodisperse under all conditions examined, despite the higher concentrations required (up to 150 μM). These measurements indicated only minor changes in shape take place upon ligand binding (Table 5).

In contrast, the SV-AUC measurements indicate a small decrease in the sedimentation coefficient on binding CO and YC-1 (Table 4). Such deviations are often interpreted as changes in protein conformation but can also be due to changes in the hydrodynamic parameters or oligomerization state.[27,64] There is no indication of dimer dissociation in these data, as evidenced by the relatively narrow sedimentation coefficient distribution obtained, nor were there indications of dissociation in the SAXS data, suggesting monomer−dimer transitions are not responsible for the observed changes. No large changes in shape were detected by SAXS upon ligand binding, suggesting that a substantial conformational change is not responsible for the observed changes in the sedimentation coefficient. The most

Table 5. Molecular Sizes Determined by SAXS

protein	complex	Guinier plot R_g (Å)[a] (quality)[b]	D_{max} (Å)	volume (Å^3)[c]
NT19	unliganded	33.7 ± 0.03 (0.93)	115	178 × 10^3
	NO	33.6 ± 0.02 (0.94)	115	–
	CO and YC-1	33.6 ± 0.03 (0.82)	115	–
NT21	unliganded	33.0 ± 0.02 (0.86)	115	135 × 10^3
	NO	32.0 ± 0.02 (0.82)	115	–
	CO and YC-1	30.7 ± 0.03 (0.80)	115	–

[a]Radius of gyration. [b]Quality score from AutoRg based upon the Guinier plot. [c]Volume of the bead model calculated by DAMAVER.

dx.doi.org/10.1021/bi301570m | *Biochemistry* XXXX, XXX, XXX−XXX

likely explanation is that binding of CO or YC-1 to *Ms* sGC NT leads to a change in the hydrodynamic properties, for example, a change in surface hydrophobicity, yielding a protein complex with altered sedimentation but with roughly the same overall conformation. Taken together, the ultracentrifugation and SAXS results indicate that the allosteric changes occurring in *Ms* sGC NT proteins upon ligand binding are small in magnitude but lead to a change in the surface properties. Consistent with this are the ~4 Å shifts observed in the *Nostoc* H-NOX domain on binding NO.[21] More complete explanations await higher-resolution models of sGC.

Chemical Cross-Linking Reveals Parallel Coiled-Coil and Domain Contacts. We undertook chemical cross-linking coupled with tandem mass spectrometry to uncover domain and subunit contacts in *Ms* sGC NT. Sixteen unique cross-linked peptides were found within the $\alpha_1\beta_1$ coiled coil. These data clearly demonstrate formation of the predicted coiled coil with parallel $\alpha_1\beta_1$ strands (Figure 5). This arrangement is in agreement with Ma and co-workers, who predicted a parallel arrangement based on electrostatic arguments despite their structure showing an antiparallel $\beta_1\beta_1$ homodimeric coiled coil for the rat sGC β_1 sequence.[23]

Nine cross-links were found between the coiled coil and other domains in *Ms* sGC NT proteins (Table 3), consistent with the coiled-coil domain serving as an organizing center. Eight of these were between the α_1 and β_1 subunits. Five additional cross-links were found between the other domains, four of which were between α_1 and β_1 subunits. Taken together, these data suggest the major interdomain contacts are between domains on opposite chains. In particular, the α_1 PAS domain appears to be closely associated with the β_1 H-NOX domain, which, in turn, is closely associated with the α_1 coiled coil.

Assembling a Model for sGC NT. Our homology models for the H-NOX and PAS domains are based upon bacterial homologues, and for the coiled-coil domain based on the numerous examples in the literature. The 62 residues linking these domains were also modeled but are of uncertain reliability because there are no homologous structures available for these regions. Additionally, we generated a homology model for the catalytic domain based on the crystal structure of the closely related adenylyl cyclase. Twenty-three intradomain cross-links were found by mass spectrometry (Table 2), all of which were consistent with the homology models, providing confidence in the reliability of these models. In particular, five unique cross-links were found in the α_1 H-NOX domain, all consistent with our homology model, supporting the prediction that it retains the H-NOX domain fold despite having lost the ability to bind heme. One cross-link each was found for the α_1 PAS and β_1 H-NOX domains. Only the β_1 PAS domain fold was unconfirmed by cross-linking.

With reliable domain models in place, we assembled and energy-minimized a domain arrangement that was consistent with our cross-linking data and our overall molecular envelopes. In this model, the parallel coiled-coil segment provides an organizing center for the other domains, particularly for the α_1 PAS and β_1 H-NOX domains, which are in contact. While there are insufficient data available for mapping residues in direct contact, two conclusions of functional importance are possible. First, although the α_1 and β_1 subunits are clearly gene duplications, sGC appears to be asymmetric. The α_1 H-NOX domain, in particular, can be removed without major effect on the overall shape while the β_1 H-NOX domain is in the center of the molecule (Figure 7). These data are consistent with those of Koglin and Behrends, who showed that a heterodimeric human sGC retains sensitivity to NO and YC-1 after deletion of the first 259 residues of the α_1 subunit.[65] Second, one face of the coiled coil is exposed in the model and may represent the cyclase domain binding surface. Such a model places the cyclase domains in contact with the β_1 H-NOX and α_1 PAS domains, in perfect position for direct regulation through ligand binding. This arrangement is consistent with two previous studies, one showing that addition of the purified β_1 H-NOX domain could inhibit sGC cyclase domains that were expressed independently, indicating direct binding,[66] and a second study making use of fluorescent fusion proteins and Förster resonance energy transfer (FRET), which concluded that the heme and catalytic domains are in the proximity of each other.[67] The model is also consistent with the α_1 and β_1 PAS domains forming part of the dimer interface, as has been suggested on the basis of homodimer formation by a bacterial homologue.[22] A cross-link between the N-termini of α_1 PAS (Lys-286) and β_1 PAS (Glu-196) constrains the domains in the model into an arrangement reminiscent of the bacterial homodimer.

Coiled-Coil Truncation Affects Proximal Histidine Release. Binding of NO to sGC yields a transient six-coordinate intermediate followed by proximal histidine release and a five-coordinate nitrosyl complex. The six-coordinate intermediate is readily observed by stopped-flow spectroscopy for both full-length sGC[68,69] and C-terminally truncated *Ms* sGC NT1 (ref 24 and Table 6). Unexpectedly, truncation of 20 additional amino acids from each chain in *Ms* sGC NT, as occurs in *Ms* sGC NT13, NT19, and NT21, yields a protein with very rapid proximal histidine release, which cannot be observed by stopped-flow spectroscopy (Table 6). Additionally, *Ms* sGC NT13, NT19, and NT21 all show tighter CO binding (Figure 1). The truncated amino acids (α_1 451−471 and β_1 381−400) are thought to complete the end of the coiled coil followed by a proline-induced turn (α_1 460 and β_1 390) and the start of a new helix, based on the β_1/β_1 coiled-coil structure.[23] The increased proximal histidine release rate in the shorter proteins suggests that the missing residues interfere with an NO-dependent change in sGC conformation. Interestingly, our cross-linking data place the α_1 PAS domain in direct contact with the C-terminal end of the coiled coil (α_1 E366−β_1 K378 cross-link) and also in direct contact with the β_1 H-NOX domain, near the heme pocket [α_1 E340−β_1 K170 and α_1 K343−β_1 K170 (Figure 4)]. This arrangement suggests the α_1 PAS domain opposes the NO-dependent conformational change in sGC. The α_1 PAS domain F helix provides the contact residues. In PAS kinase, the flexibility of the PAS domain F helix was proposed to provide inhibitory

Table 6. Histidine Release Rates for the Six-Coordinate Nitrosyl Complex[a]

Ms sGC protein	k_{6-5} (s^{-1})
NT1 (ref 24)	12.8 ± 0.4
NT1 (this work)	11.1 ± 0.5
NT2	14.5 ± 0.6
NT13	>100[b]
NT19	>100[b]
NT21	>100[b]

[a]Rate constants for proximal histidine release from the transient six-coordinate nitrosyl complex to the more stable five-coordinate nitrosyl complex. Measured at 10 °C in a stopped-flow spectrophotometer. [b]Unobserved.

dx.doi.org/10.1021/bi301570m | *Biochemistry* XXXX, XXX, XXX−XXX

interactions with adjacent domains that are relaxed upon ligand binding.[70]

A Model for Allostery in sGC Function. NO, CO, and YC-1 allosterically stimulate sGC, but how binding leads to activation remains unclear. Our data are consistent with a model in which the α_1 PAS domain inhibits binding of NO and CO to heme by enhancing their release rates. Binding of YC-1 relieves this inhibition, leading to higher CO and NO affinity (refs 24 and 25 and Figure 1). Removal of the α_1 PAS domain also relieves inhibition, yielding a heterodimeric protein with high CO affinity and a loss of YC-1 response (unpublished data[a]). Taken together, these data suggest YC-1 family compounds serve to enhance NO and CO binding by removal of an α_1 PAS domain barrier to conformational change.

Inhibition of cyclase activity is also thought to involve a direct interaction between the β_1 H-NOX domain and the cyclase domains. Winger et al. demonstrated that the isolated β_1 H-NOX domain can directly bind to the cyclase domains and inhibit cyclase activity when added in trans; they went on to suggest that binding of NO to heme in the β_1 H-NOX domain would relieve this autoinhibitory interaction.[66] Although the cyclase domains are not included in *Ms* sGC NT, our model suggests these domains may assemble onto the coiled-coil domain, opposite from where the β_1 H-NOX domain sits, allowing for direct cyclase−β_1 H-NOX domain contact. In this arrangement, the α_1 PAS domain is positioned to inhibit β_1 H-NOX, which, in turn, is positioned to inhibit cyclase. We suggest binding of YC-1 family compounds relieves the α_1 PAS domain−β_1 H-NOX domain inhibition, which in turn reduces the the level of β_1 H-NOX domain−cyclase inhibition. Binding of NO, and to a lesser extent CO, also relieves the β_1 H-NOX domain−cyclase inhibition. Binding of both would doubly oppose autoinhibition, leading to the observed synergy between binding of YC-1 and CO/NO for stimulating sGC catalysis. How YC-1 binds to sGC is not yet known but may involve binding to the α_1 PAS domain (unpublished data[a]), the β_1 H-NOX domain,[71] or both, perhaps at the α_1 PAS domain−β_1 H-NOX domain interface.

AUTHOR INFORMATION

Corresponding Author

*Department of Chemistry and Biochemistry, University of Arizona, Tucson, AZ 85721. Telephone: (520) 621-1884. Fax: (520) 626-9204. E-mail: montfort@email.arizona.edu.

Funding

This work was supported by National Institutes of Health Grants HL062969 and GM077390 (W.R.M.), GM051387 (V.H.W.), and T32 GM008804 (B.G.F.), American Heart Association Grant 10PRE2630177 (B.G.F.), and National Science Foundation Grant 0744732 (F.T.). Orbitrap mass spectrometry data were acquired by the Arizona Proteomics Consortium at the University of Arizona, supported by National Center for Research Resources (NCRR) Grant S10 RR028868-01. SAXS measurements were taken at the Stanford Synchrotron Radiation Lightsource, supported by the Department of Energy and by the National Institutes of Health (NCRR and National Institute of General Medical Sciences).

Notes

The authors declare no competing financial interest.

ACKNOWLEDGMENTS

We are deeply grateful to Dr. Thomas Weiss and Dr. Tsutomu Matsui (Stanford Synchrotron Radiation Laboratory, Menlo Park, CA) for assistance with collection and interpretation of SAXS data and to Dr. Katrina Miranda for providing DEA/NO. We thank Dr. Ah-Lim Tsai and Dr. Vladimir Berka (University of Houston, Houston, TX) for preliminary kinetic measurements of NT13 indicating rapid loss of the proximal histidine upon NO binding. We thank Dr. Chad Park for assistance with ultracentrifugation measurements. Portions of this research were conducted at the Stanford Synchrotron Radiation Lightsource (SSRL), a national user facility operated by Stanford University on behalf of the U.S. Department of Energy, Office of Basic Energy Sciences. The SSRL Structural Molecular Biology Program is supported by the Department of Energy, Office of Biological and Environmental Research, and by the National Institutes of Health, National Center for Research Resources, Biomedical Technology Program.

ABBREVIATIONS

YC-1, 3-(5′-hydroxymethyl-2′-furyl)-1-benzylindazole; BS^2G, bis(sulfosuccinimidyl)glutarate-d_0; BS3, bis(sulfosuccinimidyl)-suberate-d_0; EDC, 1-ethyl-3-[3-(dimethylamino)propyl]-carbodiimide hydrochloride; BMOE, bis(maleimido)ethane; SAXS, small-angle X-ray scattering; DLS, dynamic light scattering; SV-AUC, sedimentation velocity analytical ultracentrifugation; *Ms*, *M. sexta*.

ADDITIONAL NOTE

[a]Rahul Purohit, Bradley G. Fritz, Andrzej Weichsel, Juliana The, Eric Campbell, Leida Rassouli-Taylor, Elsa D. Garcin, Matthew J. Gage and William R. Montfort, manuscript in preparation.

REFERENCES

(1) Ignarro, L. J., Ed. (2010) *Nitric Oxide Biology and Pathobiology*, 2nd ed., Academic Press, San Diego.

(2) Li, H., and Poulos, T. L. (2005) Structure-function studies on nitric oxide synthases. *J. Inorg. Biochem. 99*, 293−305.

(3) Stuehr, D. J., Tejero, J., and Haque, M. M. (2009) Structural and mechanistic aspects of flavoproteins: Electron transfer through the nitric oxide synthase flavoprotein domain. *FEBS J. 276*, 3959−3974.

(4) Derbyshire, E. R., and Marletta, M. A. (2012) Structure and regulation of soluble guanylate cyclase. *Annu. Rev. Biochem. 81*, 533−559.

(5) Schulz, R., Rassaf, T., Massion, P. B., Kelm, M., and Balligand, J. L. (2005) Recent advances in the understanding of the role of nitric oxide in cardiovascular homeostasis. *Pharmacol. Ther. 108*, 225−256.

(6) Pyriochou, A., and Papapetropoulos, A. (2005) Soluble guanylyl cyclase: More secrets revealed. *Cell. Signalling 17*, 407−413.

(7) Roger, V. L., Go, A. S., Lloyd-Jones, D. M., Benjamin, E. J., Berry, J. D., Borden, W. B., Bravata, D. M., Dai, S., Ford, E. S., Fox, C. S., Fullerton, H. J., Gillespie, C., Hailpern, S. M., Heit, J. A., Howard, V. J., Kissela, B. M., Kittner, S. J., Lackland, D. T., Lichtman, J. H., Lisabeth, L. D., Makuc, D. M., Marcus, G. M., Marelli, A., Matchar, D. B., Moy, C. S., Mozaffarian, D., Mussolino, M. E., Nichol, G., Paynter, N. P., Soliman, E. Z., Sorlie, P. D., Sotoodehnia, N., Turan, T. N., Virani, S. S., Wong, N. D., Woo, D., and Turner, M. B. (2012) Heart disease and stroke statistics—2012 update: A report from the American Heart Association. *Circulation 125*, e2−e220.

(8) Murrell, W. (1879) Nitro-glycerine as a remedy for angina pectoris. *Lancet 113*, 113−115.

(9) Evgenov, O. V., Pacher, P., Schmidt, P. M., Hasko, G., Schmidt, H. H., and Stasch, J. P. (2006) NO-independent stimulators and activators of soluble guanylate cyclase: Discovery and therapeutic potential. *Nat. Rev. Drug Discovery 5*, 755−768.

(10) Belik, J. (2009) Riociguat, an oral soluble guanylate cyclase stimulator for the treatment of pulmonary hypertension. *Curr. Opin. Invest. Drugs 10*, 971−979.

(11) Mittendorf, J., Weigand, S., Alonso-Alija, C., Bischoff, E., Feurer, A., Gerisch, M., Kern, A., Knorr, A., Lang, D., Muenter, K., Radtke, M., Schirok, H., Schlemmer, K. H., Stahl, E., Straub, A., Wunder, F., and Stasch, J. P. (2009) Discovery of riociguat (BAY 63-2521): A potent, oral stimulator of soluble guanylate cyclase for the treatment of pulmonary hypertension. *ChemMedChem 4*, 853−865.
(12) Martin, F., Baskaran, P., Ma, X., Dunten, P. W., Schaefer, M., Stasch, J. P., Beuve, A., and van den Akker, F. (2010) Structure of cinaciguat (BAY 58-2667) bound to *Nostoc* H-NOX domain reveals insights into heme-mimetic activation of the soluble guanylyl cyclase. *J. Biol. Chem. 285*, 22651−22657.
(13) Meurer, S., Pioch, S., Pabst, T., Opitz, N., Schmidt, P. M., Beckhaus, T., Wagner, K., Matt, S., Gegenbauer, K., Geschka, S., Karas, M., Stasch, J. P., Schmidt, H. H., and Muller-Esterl, W. (2009) Nitric oxide-independent vasodilator rescues heme-oxidized soluble guanylate cyclase from proteasomal degradation. *Circ. Res. 105*, 33−41.
(14) Taqatqeh, F., Mergia, E., Neitz, A., Eysel, U. T., Koesling, D., and Mittmann, T. (2009) More than a retrograde messenger: Nitric oxide needs two cGMP pathways to induce hippocampal long-term potentiation. *J. Neurosci. 29*, 9344−9350.
(15) Cary, S. P., Winger, J. A., Derbyshire, E. R., and Marletta, M. A. (2006) Nitric oxide signaling: No longer simply on or off. *Trends Biochem. Sci. 31*, 231−239.
(16) Moglich, A., Ayers, R. A., and Moffat, K. (2009) Structure and signaling mechanism of Per-ARNT-Sim domains. *Structure 17*, 1282−1294.
(17) Friebe, A., Schultz, G., and Koesling, D. (1996) Sensitizing soluble guanylyl cyclase to become a highly CO-sensitive enzyme. *EMBO J. 15*, 6863−6868.
(18) Stone, J. R., and Marletta, M. A. (1998) Synergistic activation of soluble guanylate cyclase by YC-1 and carbon monoxide: Implications for the role of cleavage of the iron-histidine bond during activation by nitric oxide. *Chem. Biol. 5*, 255−261.
(19) Pellicena, P., Karow, D. S., Boon, E. M., Marletta, M. A., and Kuriyan, J. (2004) Crystal structure of an oxygen-binding heme domain related to soluble guanylate cyclases. *Proc. Natl. Acad. Sci. U.S.A. 101*, 12854−12859.
(20) Nioche, P., Berka, V., Vipond, J., Minton, N., Tsai, A. L., and Raman, C. S. (2004) Femtomolar sensitivity of a NO sensor from *Clostridium botulinum*. *Science 306*, 1550−1553.
(21) Ma, X., Sayed, N., Beuve, A., and van den Akker, F. (2007) NO and CO differentially activate soluble guanylyl cyclase via a heme pivot-bend mechanism. *EMBO J. 26*, 578−588.
(22) Ma, X., Sayed, N., Baskaran, P., Beuve, A., and van den Akker, F. (2008) PAS-mediated Dimerization of Soluble Guanylyl Cyclase Revealed by Signal Transduction Histidine Kinase Domain Crystal Structure. *J. Biol. Chem. 283*, 1167−1178.
(23) Ma, X., Beuve, A., and van den Akker, F. (2010) Crystal structure of the signaling helix coiled-coil domain of the β1 subunit of the soluble guanylyl cyclase. *BMC Struct. Biol. 10*, 2.
(24) Hu, X., Murata, L. B., Weichsel, A., Brailey, J. L., Roberts, S. A., Nighorn, A., and Montfort, W. R. (2008) Allostery in recombinant soluble guanylyl cyclase from *Manduca sexta*. *J. Biol. Chem. 283*, 20968−20977.
(25) Hu, X., Feng, C., Hazzard, J. T., Tollin, G., and Montfort, W. R. (2008) Binding of YC-1 or BAY 41-2272 to Soluble Guanylyl Cyclase Induces a Geminate Phase in CO Photolysis. *J. Am. Chem. Soc. 130*, 15748−15749.
(26) Fritz, B. G., Hu, X., Brailey, J. L., Berry, R. E., Walker, F. A., and Montfort, W. R. (2011) Oxidation and loss of heme in soluble guanylyl cyclase from *Manduca sexta*. *Biochemistry 50*, 5813−5815.
(27) Schuck, P. (2000) Size-distribution analysis of macromolecules by sedimentation velocity ultracentrifugation and Lamm equation modeling. *Biophys. J. 78*, 1606−1619.
(28) Lebowitz, J., Lewis, M. S., and Schuck, P. (2002) Modern analytical ultracentrifugation in protein science: A tutorial review. *Protein Sci. 11*, 2067−2079.
(29) Shevchenko, A., Wilm, M., Vorm, O., and Mann, M. (1996) Mass spectrometric sequencing of proteins silver-stained polyacrylamide gels. *Anal. Chem. 68*, 850−858.
(30) Li, W., O'Neill, H. A., and Wysocki, V. H. (2012) SQID-XLink: Implementation of an intensity-incorporated algorithm for cross-linked peptide identification. *Bioinformatics 28*, 2548−2550.
(31) Chalkley, R. J., Baker, P. R., Medzihradszky, K. F., Lynn, A. J., and Burlingame, A. L. (2008) In-depth analysis of tandem mass spectrometry data from disparate instrument types. *Mol. Cell. Proteomics 7*, 2386−2398.
(32) Smolsky, I. L., Liu, P., Niebuhr, M., Ito, K., Weiss, T. M., and Tsuruta, H. (2007) Biological small-angle X-ray scattering facility at the Stanford Synchrotron Radiation Laboratory. *J. Appl. Crystallogr. 40*, S453−S458.
(33) Orthaber, D., Bergmann, A., and Glatter, O. (2000) SAXS experiments on absolute scale with Kratky systems using water as a secondary standard. *J. Appl. Crystallogr. 33*, 218−225.
(34) Svergun, D. I., Konarev, P. V., Volkov, V. V., Sokolova, A. V., and Koch, M. H. J. (2003) PRIMUS: A Windows PC-based system for small-angle scattering data analysis. *J. Appl. Crystallogr. 36*, 1277−1282.
(35) Svergun, D. I. (1992) Determination of the Regularization Parameter in Indirect-Transform Methods Using Perceptual Criteria. *J. Appl. Crystallogr. 25*, 495−503.
(36) Petoukhov, M. V., Konarev, P. V., Kikhney, A. G., and Svergun, D. I. (2007) ATSAS 2.1: Towards automated and web-supported small-angle scattering data analysis. *J. Appl. Crystallogr. 40*, S223−S228.
(37) Svergun, D. I. (1999) Restoring low resolution structure of biological macromolecules from solution scattering using simulated annealing. *Biophys. J. 76*, 2879−2886.
(38) Volkov, V. V., and Svergun, D. I. (2003) Uniqueness of ab initio shape determination in small-angle scattering. *J. Appl. Crystallogr. 36*, 860−864.
(39) Demeler, B. (2005) UltraScan: A Comprehensive Data Analysis Software Package for Analytical Ultracentrifugation Experiments. In *Analytical Ultracentrifugation: Techniques and Methods* (Scott, D. J., Harding, S. E., and Rowe, A. J., Eds.) pp 210−229, The Royal Society of Chemistry, Cambridge, U.K.
(40) Svergun, D., Barberato, C., and Koch, M. H. J. (1995) CRYSOL: A program to evaluate X-ray solution scattering of biological macromolecules from atomic coordinates. *J. Appl. Crystallogr. 28*, 768−773.
(41) Pettersen, E. F., Goddard, T. D., Huang, C. C., Couch, G. S., Greenblatt, D. M., Meng, E. C., and Ferrin, T. E. (2004) UCSF Chimera: A visualization system for exploratory research and analysis. *J. Comput. Chem. 25*, 1605−1612.
(42) Ginalski, K., Elofsson, A., Fischer, D., and Rychlewski, L. (2003) 3D-Jury: A simple approach to improve protein structure predictions. *Bioinformatics 19*, 1015−1018.
(43) Kim, D. E., Chivian, D., and Baker, D. (2004) Protein structure prediction and analysis using the Robetta server. *Nucleic Acids Res. 32*, W526−W531.
(44) Chen, R., Li, L., and Weng, Z. (2003) ZDOCK: An initial-stage protein-docking algorithm. *Proteins 52*, 80−87.
(45) Noel, J. K., Whitford, P. C., Sanbonmatsu, K. Y., and Onuchic, J. N. (2010) SMOG@ctbp: Simplified deployment of structure-based models in GROMACS. *Nucleic Acids Res. 38*, W657−W661.
(46) Whitford, P. C., Noel, J. K., Gosavi, S., Schug, A., Sanbonmatsu, K. Y., and Onuchic, J. N. (2009) An all-atom structure-based potential for proteins: Bridging minimal models with all-atom empirical forcefields. *Proteins 75*, 430−441.
(47) Grubisic, I., Shokhirev, M. N., Orzechowski, M., Miyashita, O., and Tama, F. (2010) Biased coarse-grained molecular dynamics simulation approach for flexible fitting of X-ray structure into cryo electron microscopy maps. *J. Struct. Biol. 169*, 95−105.
(48) Ahmed, A., Whitford, P. C., Sanbonmatsu, K. Y., and Tama, F. (2012) Consensus among flexible fitting approaches improves the interpretation of cryo-EM data. *J. Struct. Biol. 177*, 561−570.

(49) Van Der Spoel, D., Lindahl, E., Hess, B., Groenhof, G., Mark, A. E., and Berendsen, H. J. (2005) GROMACS: Fast, flexible, and free. *J. Comput. Chem. 26*, 1701−1718.
(50) Pierce, B., and Weng, Z. (2007) ZRANK: Reranking protein docking predictions with an optimized energy function. *Proteins 67*, 1078−1086.
(51) Weast, R. C., Ed. (1989) *CRC Handbook of Chemistry and Physics*, 70th ed., CRC Press, Inc., Boca Raton, FL.
(52) Sinz, A. (2006) Chemical cross-linking and mass spectrometry to map three-dimensional protein structures and protein-protein interactions. *Mass Spectrom. Rev. 25*, 663−682.
(53) Mertens, H. D., and Svergun, D. I. (2010) Structural characterization of proteins and complexes using small-angle X-ray solution scattering. *J. Struct. Biol. 172*, 128−141.
(54) Rambo, R. P., and Tainer, J. A. (2010) Bridging the solution divide: Comprehensive structural analyses of dynamic RNA, DNA, and protein assemblies by small-angle X-ray scattering. *Curr. Opin. Struct. Biol. 20*, 128−137.
(55) Rambo, R. P., and Tainer, J. A. (2011) Characterizing flexible and intrinsically unstructured biological macromolecules by SAS using the Porod-Debye law. *Biopolymers 95*, 559−571.
(56) Eswar, N., Webb, B., Marti-Renom, M. A., Madhusudhan, M. S., Eramian, D., Shen, M. Y., Pieper, U., and Sali, A. (2006) Comparative protein structure modeling using Modeller. *Current Protocols in Bioinformatics*, Chapter 5, Unit 5.6, Wiley, New York.
(57) Friebe, A., Mullershausen, F., Smolenski, A., Walter, U., Schultz, G., and Koesling, D. (1998) YC-1 potentiates nitric oxide- and carbon monoxide-induced cyclic GMP effects in human platelets. *Mol. Pharmacol. 54*, 962−967.
(58) Ramanathan, S., Mazzalupo, S., Boitano, S., and Montfort, W. R. (2011) Thrombospondin-1 and angiotensin II inhibit soluble guanylyl cyclase through an increase in intracellular calcium concentration. *Biochemistry 50*, 7787−7799.
(59) Zhou, Z., Sayed, N., Pyriochou, A., Roussos, C., Fulton, D., Beuve, A., and Papapetropoulos, A. (2008) Protein kinase G phosphorylates soluble guanylyl cyclase on serine 64 and inhibits its activity. *Arterioscler., Thromb., Vasc. Biol. 28*, 1803−1810.
(60) Meurer, S., Pioch, S., Gross, S., and Muller-Esterl, W. (2005) Reactive oxygen species induce tyrosine phosphorylation of and Src kinase recruitment to NO-sensitive guanylyl cyclase. *J. Biol. Chem. 280*, 33149−33156.
(61) Kharitonov, V. G., Russwurm, M., Magde, D., Sharma, V. S., and Koesling, D. (1997) Dissociation of nitric oxide from soluble guanylate cyclase. *Biochem. Biophys. Res. Commun. 239*, 284−286.
(62) Russwurm, M., and Koesling, D. (2004) NO activation of guanylyl cyclase. *EMBO J. 23*, 4443−4450.
(63) Winger, J. A., Derbyshire, E. R., and Marletta, M. A. (2007) Dissociation of nitric oxide from soluble guanylate cyclase and heme-nitric oxide/oxygen binding domain constructs. *J. Biol. Chem. 282*, 897−907.
(64) Zhao, H., Balbo, A., Brown, P. H., and Schuck, P. (2011) The boundary structure in the analysis of reversibly interacting systems by sedimentation velocity. *Methods 54*, 16−30.
(65) Koglin, M., and Behrends, S. (2003) A functional domain of the α1 subunit of soluble guanylyl cyclase is necessary for activation of the enzyme by nitric oxide and YC-1 but is not involved in heme binding. *J. Biol. Chem. 278*, 12590−12597.
(66) Winger, J. A., and Marletta, M. A. (2005) Expression and characterization of the catalytic domains of soluble guanylate cyclase: Interaction with the heme domain. *Biochemistry 44*, 4083−4090.
(67) Haase, T., Haase, N., Kraehling, J. R., and Behrends, S. (2010) Fluorescent fusion proteins of soluble guanylyl cyclase indicate proximity of the heme nitric oxide domain and catalytic domain. *PLoS One 5*, e11617.
(68) Zhao, Y., Brandish, P. E., Ballou, D. P., and Marletta, M. A. (1999) A molecular basis for nitric oxide sensing by soluble guanylate cyclase. *Proc. Natl. Acad. Sci. U.S.A. 96*, 14753−14758.
(69) Martin, E., Berka, V., Sharina, I., and Tsai, A. L. (2012) Mechanism of binding of NO to soluble guanylyl cyclase: Implication for the second NO binding to the heme proximal site. *Biochemistry 51*, 2737−2746.
(70) Amezcua, C. A., Harper, S. M., Rutter, J., and Gardner, K. H. (2002) Structure and interactions of PAS kinase N-terminal PAS domain: Model for intramolecular kinase regulation. *Structure 10*, 1349−1361.
(71) Yoo, B. K., Lamarre, I., Rappaport, F., Nioche, P., Raman, C. S., Martin, J. L., and Negrerie, M. (2012) Picosecond to Second Dynamics Reveals a Structural Transition in *Clostridium botulinum* NO-Sensor Triggered by the Activator BAY-41-2272. *ACS Chem. Biol. 7*, 2046−2054.